

Visual enhancement of Cone-beam CT by use of CycleGAN

S Kida^{†1}, S Kaji^{‡1}, K Nawa[†], T Imae[†], T Nakamoto[†], S Ozaki[†], T Ohta[†], Y Nozawa[†] and K Nakagawa[†]

[†] Department of Radiology, University of Tokyo Hospital, 7-3-1, Hongo, Bunkyo-ku, Tokyo 113-0033, Japan

[‡] Institute of Mathematics for Industry, Kyushu University, 744 Motooka, Nishi-ku, Fukuoka 819-0395, Japan / JST PRESTO

Author to whom correspondence should be addressed. email: skaji@imi.kyushu-u.ac.jp

Abstract

Purpose: Cone-beam computed tomography (CBCT) offers advantages over conventional fan-beam CT in that it requires a shorter time and less exposure to obtain images. However, CBCT images suffer from low soft-tissue contrast, noise, and artifacts compared to conventional fan-beam CT images. Therefore, it is essential to improve the image quality of CBCT.

Methods: In this paper, we propose a synthetic approach to translate CBCT images with deep neural networks. Our method requires only unpaired and unaligned CBCT images and planning fan-beam CT (PlanCT) images for training. The CBCT images and PlanCT images may be obtained from other patients as long as they are acquired with the same scanner settings. Once trained, three-dimensionally reconstructed CBCT images can be directly translated to high-quality PlanCT-like images.

Results: We demonstrate the effectiveness of our method with images obtained from 24 prostate patients, and provide a statistical and visual comparison. The image quality of the translated images shows substantial improvement in voxel values, spatial uniformity, and artifact suppression compared to those of the original CBCT. The anatomical structures of the original CBCT images were also well preserved in the translated images.

Conclusions: Our method produces visually PlanCT-like images from CBCT images while preserving anatomical structures.

1. Introduction

Cone-beam computed tomography (CBCT) uses a wide, cone-beam of X-rays and offers considerable advantages insofar as the volume information of patients can be obtained more quickly and with lower exposure. Compared to conventional fan-beam CT, however, the image quality of CBCT is degraded due to X-ray scattering and truncated projections, hindering the effective use of CBCT in many potential applications. It is therefore important to improve the image quality of CBCT.

The most popular use of CBCT in modern radiation therapy is for patient positioning in image-guided radiation therapy^{1,2,3,4}. CBCT imaging systems can be incorporated into a conventional

¹Kida and Kaji should be considered joint first authors.

radiotherapy device, since they are inexpensive and compact. Usually, planning fan-beam CT (PlanCT) images with high resolution for treatment planning in radiation therapy are acquired once before the course of treatment. On the other hand, CBCT images are acquired just before each radiation treatment along the fractional irradiations on the treatment couch to provide up-to-date anatomical information regarding the patients. Patient setup for radiation therapy is performed by manual or automatic image registration between CBCT and PlanCT using target registration software. However, the quality of image registration often depends on the experience and intuition of the operator, because the image quality of CBCT is insufficient for identifying the structure of organs within soft tissue. Recently, possible applications of CBCT for patient-specific treatment have also been explored. The CBCT images acquired during each treatment can include information on the patient's condition and the response to the treatment. Several methods of quantitative radiomic analysis using CBCT have been reported^{5,6}. However, the low image quality of CBCT may prevent the accurate extraction of such radiomic information. The effective use of CBCT for adaptive radiation therapy (ART) has also been studied. In addition to CBCT, many approaches to the implementation of ART have been investigated that allow adaptive treatment change based on patient anatomy. Although CBCT images provide up-to-date information regarding patients, they have not been used directly to compute dose distributions for re-planning in ART owing to their low image quality^{7,8}. The conventional approach to dose calculation using CBCT is to transform PlanCT images to CBCT images using deformable image registration (DIR) and then calculate the dose distribution using the transformed PlanCT^{9,10,11}. Another approach to dose calculation using CBCT is to compute the dose distribution directly with the improved CBCT images¹². Improving the CBCT image quality while preserving the anatomical structures of CBCT should be effective for both approaches.

It is essential to improve the image quality of CBCT image for the overall accuracy of radiotherapy. Several methods have been applied to remove the scatter photons from CBCT 2D projection images, such as hardware suppression using an anti-scatter grid and software estimation using a scatter deconvolution technique^{12,13,14}. On the other hand, a different approach has been proposed, which uses PlanCT as prior information to improve the quality of CBCT images. This approach is applicable to direct 3D image reconstruction with sparse sampling¹⁵, histogram matching¹⁶, super-resolution¹⁷, and a deep convolutional neural network¹⁸. Although these do not require access to the raw projection data or a particular scanner manufacturer, they depend on accurate spatial alignment of CBCT and PlanCT volume pairs from the same patients. Misalignments between paired images can lead to errors like edge blurring, deformation, and the disappearance of some anatomical structures in the improved CBCT images. However, it is challenging to achieve

sufficiently accurate alignments between CBCT and PlanCT images even for the same patient, because these images are clinically acquired on different days separated by days or weeks.

Deep neural networks (DNNs) have been successfully applied to various image processing tasks^{19,20}. In particular, the generative adversarial network (GAN) has been widely used for image-to-image translation²¹. Nie et al. have applied the idea of combining voxel-wise loss with adversarial loss to translating brain MRI to CT images. As a result, high-quality, less blurry CT images were synthesized²². However, voxel-wise loss also depends on the accuracy of the alignment of paired images, and it is clinically difficult, if not impossible, to acquire aligned paired training images from two different modalities. To learn the translation mappings in the absence of aligned paired images, a cycle-consistency GAN (CycleGAN)²³ has been proposed. Recently, CycleGAN has been used to synthesize CT images from MR images^{22,24}, and to synthesize CT images from CBCT images²⁵.

Suppose we have two sets of images from two domains, X and Y . It should be emphasized that we do not require any prescribed correspondence between the elements of X and Y . To translate CBCT and PlanCT images, we need only independent images from CBCT and PlanCT, and these may be taken on different days from different patients. We only require that each set is consistent and uniform; the images in each set are acquired with the same scanner setting and contain similar parts of the body. CycleGAN learns a mapping $G_{X \rightarrow Y} : X \rightarrow Y$ and $G_{Y \rightarrow X} : Y \rightarrow X$, such that the distributions (or characteristics) of images from the output of $G_{X \rightarrow Y}$ (and, respectively, of $G_{Y \rightarrow X}(Y)$) are indistinguishable from that of Y (and, respectively, X) using an adversarial loss. In addition, a cycle-consistency loss is introduced to force the network to translate the synthesized image back to the original image domain and minimize the difference between the original input image and the reproduced image. This scheme has intrinsic ambiguity with respect to geometric transformation, which may fail to preserve the anatomical structure in transformed medical images.

In this paper, we propose a synthetic approach to producing PlanCT-like images (SynPlanCT images) from CBCT images. The proposed method relies exclusively on unpaired and unaligned image datasets. The proposed approach is based on CycleGAN with modifications tailored for this specific task. The network structure and the loss functions were determined through trial and error while observing the image quality of the SynPlanCT images. In addition to the image quality, we paid a particular attention to structure preservation. We devised a few tricks to enforce boundary-preservation (typically, that of bone and air), which clinicians rely on for image registration. The image quality of SynPlanCT images was quantitatively evaluated in terms of their voxel values and spatial uniformity. We analyzed the extent to which they preserved the anatomical structures through a comparison with the original CBCT images, and the corresponding PlanCT images

aligned to the CBCT images by the deformable image registration. The robustness of our method was confirmed by investigating SynPlanCT images from five network models trained with the same structure and hyper-parameter settings.

The remainder of this paper is organized as follows. In §II., we explain how we collected and processed image data to train our neural networks, and we provide details regarding the neural networks based on CycleGAN. We also discuss the evaluation of our method, which is based on comparing the ROI from the images. In §III., we present the output of our method and some statistics related to its evaluation. In §IV., we focus on the evaluation, specifically the robustness of our method and its improvement in image quality. In §V., we summarize our findings.

II. Materials and Methods

II.A. Data acquisition and image processing

In this study, we used CBCT and PlanCT images from prostate cancer patients who underwent stereotactic radiotherapy with an Elekta Synergy linear accelerator (Elekta AB, Stockholm, Sweden). The PlanCT images were acquired on a 16-row multidetector helical CT scanner with a tube voltage of 120 kV, a tube current of 350 mA, a gantry rotation time of 0.5 s, a matrix size of 512 by 512 on the axial plane with a pixel size of 1.074 mm by 1.074 mm and a slice thickness of 1 mm. The PlanCT images were reconstructed by an analytical reconstruction method in the form of filtered backprojection (FBP). The CBCT images were acquired during the course of the treatment using a kV on-board imager (XVI) with a tube voltage 120 kV, a tube current 40 mA/frame, and an exposure time 40 ms/frame. For each scan, in total, 360 projections were acquired in a full-scan (360° gantry rotation). The CBCT reconstructions were performed by the analytical reconstruction method in the form of FBP using projection images of one imaging panel shifted to 11.5 cm to encompass the target. These were output to match the resolution and the slice thickness of the PlanCT images automatically using XVI. For 20 patients, the PlanCT images were acquired only once, about two weeks before the course of treatment. Among the images from the 20 patients, those from 4 patients (referred to hereafter as (i)–(iv)) were kept for evaluation, and those from the remaining 16 patients were used to train the network. In addition, there were 4 patients from whom PlanCT images was acquired just after the acquisition of the CBCT images (they are referred to hereafter as patient (v)–(viii)). In those CBCT and PlanCT images, the anatomical structures were relatively close. We transformed the PlanCT images to align with the CBCT images by a deformable image registration using RayStation (v4.6, RaySearch Laboratories). We used these deformed PlanCT images (hereafter, they are referred to as DefPlanCT images) for evaluation.

Ideally, the result of our method should be evaluated using the CBCT and PlanCT images, which are acquired at the same time, and thus make a perfectly matched pair. Such a pair is virtually impossible to obtain, and we suppose that our DefPlanCT is a reasonable alternative. We used a total of 2795 CBCT images and 2795 PlanCT images for training, although these numbers need not be same.

Preprocessing to obtain training CBCT and PlanCT images was performed as follows. To prevent any adverse impacts from non-anatomical structures (treatment couch and other objects outside the body) on a CBCT-to-PlanCT registration and as a model training procedure, binary masks were created to separate the pelvic region from the non-anatomical regions. These masks were generated by applying the Otsu auto-thresholding method²⁶ on each CBCT and PlanCT image. The voxel values outside the mask region were entirely replaced with a Hounsfield Unit (HU) of -1000. Then, the masked PlanCT volume data for each patient were three-dimensionally pre-aligned to each of the masked CBCT images by rigid registration using an open-source software called Elastix²⁷. Though CycleGAN does not require exactly aligned paired images of CBCT and PlanCT, three-dimensional (3D) pre-alignment was performed such that the bodies of all patients were included in a cropped calculation area around the center with a size of 480×384 pixels for efficient calculation.

II.B. Image synthesis with deep neural network

We regard a (volumetric) CT image in any modality as an array $\mathbb{R}^{h \times w \times d}$, where $h \times w$ is the slice dimension and d is the number of slices. Image synthesis (or conversion) can be considered as a mapping $\mathbb{R}^{h_1 \times w_1 \times d_1} \rightarrow \mathbb{R}^{h_2 \times w_2 \times d_2}$, which takes an image of size $h_1 \times w_1$ and d_1 channels/slices (a CBCT image, in our particular case) and outputs another of size $h_2 \times w_2$ and d_2 channels/slices (a PlanCT image, in our case). We assume that $h_1 = h_2 = h$ and $w_1 = w_2 = w$ by resizing the images if necessary. A popular way to construct such a mapping is to use a DNN that learns (i.e., is trained) to construct mappings from a large set of data. The problem of synthesizing a PlanCT image that corresponds to a given CBCT image is highly ill-posed. That is, there is no unique “best” way to find the solution. Thus, we define what constitutes bad mappings in a quantitative way in terms of a loss function, whereby the DNN finds an approximate mapping that minimizes the loss function.

Due to computational limitations, we assume that the conversion mapping is uniform along the third dimension such that it can be approximated by a mapping $\mathbb{R}^{h \times w} \rightarrow \mathbb{R}^{h \times w}$. That is, our mapping converts CT images slice-by-slice along the z -axis.

Our strategy is largely based on CycleGAN²³, which simultaneously constructs four mappings:

(i) a generator $G_{C \rightarrow P} : \mathbb{R}^{h \times w} \rightarrow \mathbb{R}^{h \times w}$, which takes a CBCT image and outputs a synthesized PlanCT image, (ii) a generator $G_{P \rightarrow C} : \mathbb{R}^{h \times w} \rightarrow \mathbb{R}^{h \times w}$, which takes a PlanCT image and outputs a synthesized CBCT image, (iii) a discriminator $D_P : \mathbb{R}^{h \times w} \rightarrow \mathbb{R}^{h' \times w'}$, which distinguishes synthesized PlanCT images from real ones (iv) and a discriminator $D_C : \mathbb{R}^{h \times w} \rightarrow \mathbb{R}^{h' \times w'}$, which distinguishes synthesized CBCT images from real ones. The discriminator D_P looks at (overlapping) patches in a whole slice and determines whether each patch is likely to be one from a real image. Ideally, D_P would output the all-zero array $\mathbf{0}$ for synthesized PlanCT images and the all-one array $\mathbf{1}$ for real PlanCT images. The discriminator D_C works similarly for real and synthesized CBCT images. We approximate these mappings by training a DNN for each mapping from a set **Plan** of PlanCT images and a set **CB** of CBCT images. To this end, we formulate the desired properties of the mappings in terms of loss functions. Generators and discriminators have different sets of goals, and hence, different loss functions. Let $\|v\|_p$ denote the L^p -norm of a vector v . Our loss function for the discriminators is based on LSGAN²⁸.

$$\begin{aligned} \text{Loss}_D = & \lambda_D \sum_{x \in \mathbf{CB}} (\|D_P(G_{C \rightarrow P}(x)) - \mathbf{0}\|_2 + \|D_C(x) - \mathbf{1}\|_2) \\ & + \lambda_D \sum_{y \in \mathbf{Plan}} (\|D_C(G_{P \rightarrow C}(y)) - \mathbf{0}\|_2 + \|D_P(y) - \mathbf{1}\|_2). \end{aligned}$$

The loss function forces D_P (and, respectively, D_C) to be trained to distinguish the distributions of real PlanCT (and, respectively, CBCT) images from synthesized ones.

Our loss function for generators $G_{C \rightarrow P}$ and $G_{P \rightarrow C}$ consists of several terms:

- $\text{Loss}_{\text{cycle}} = \text{Loss}_{\text{cycle}A} + \text{Loss}_{\text{cycle}B}$, where $\text{Loss}_{\text{cycle}A} = \sum_{x \in \mathbf{CB}} \|x - G_{P \rightarrow C}(G_{C \rightarrow P}(x))\|_1$, $\text{Loss}_{\text{cycle}B} = \sum_{y \in \mathbf{Plan}} \|y - G_{C \rightarrow P}(G_{P \rightarrow C}(y))\|_1$. This is the cycle-consistency loss which ensures that $G_{C \rightarrow P}$ and $G_{P \rightarrow C}$ are inverse mappings with respect to each other.
- $\text{Loss}_{\text{adv}} = \sum_{x \in \mathbf{CB}} \|D_P(G_{C \rightarrow P}(x)) - \mathbf{1}\|_2 + \sum_{y \in \mathbf{Plan}} \|D_C(G_{P \rightarrow C}(y)) - \mathbf{1}\|_2$: This encourages the generators to fool the discriminators by synthesizing realistic images.
- $\text{Loss}_{\text{tv}} = \sum_{x \in \mathbf{CB}} \|\text{grad}G_{C \rightarrow P}(x)\|_1$, where grad is the image gradient. This is the total variation regularization which encourages the generator to produce spatially uniform images. Since even the real images in **CB** are noisy, we apply this loss only to $G_{C \rightarrow P}(x)$ which are the SynPlanCT images.
- $\text{Loss}_{\text{air}} = \sum_{x \in \mathbf{CB}} \|\psi(G_{C \rightarrow P}(x)) - \psi(x)\|_1 + \sum_{y \in \mathbf{Plan}} \|\psi(G_{P \rightarrow C}(y)) - \psi(y)\|_1$, where $\psi(z) = \begin{cases} z & (z < C) \\ 0 & (z \geq C) \end{cases}$, where C is a constant equivalent to -465 HU. This enforces the generators not to alter air regions having low values less than -465 HU to preserve the air-body boundary.

- $\text{Loss}_{grad} = \sum_{x \in \mathbf{CB}} (\|\partial_1(x - G_{C \rightarrow P}(x))\|_2 + \|\partial_2(x - G_{C \rightarrow P}(x))\|_2) + \sum_{y \in \mathbf{Plan}} (\|\partial_1(y - G_{P \rightarrow C}(y))\|_2 + \|\partial_2(y - G_{P \rightarrow C}(y))\|_2)$, where (∂_1, ∂_2) is Sobel’s approximated gradient operator²⁹. This encourages structural preservation before and after conversion by trying to keep the edges in the image.
- $\text{Loss}_{idem} = \sum_{x \in \mathbf{CB}} \|G_{C \rightarrow P}(x) - G_{C \rightarrow P}(G_{C \rightarrow P}(x))\|_1 + \sum_{y \in \mathbf{Plan}} \|G_{P \rightarrow C}(y) - G_{P \rightarrow C}(G_{P \rightarrow C}(y))\|_1$: This ensures that $G_{C \rightarrow P}^2 = G_{C \rightarrow P}$ and $G_{P \rightarrow C}^2 = G_{P \rightarrow C}$ (i.e., that they are idempotent).

The terms Loss_{cycle} and Loss_{idem} pertain to mathematical requirements regarding what the conversion mappings should satisfy, and they help to increase the stability during training. The terms Loss_{grad} and Loss_{adv} are competing demands as the former stipulates that the generator preserves the structure of the input image while the latter encourages altering the input image to look more like a real one. In the end, they should find a good balance. Note that Loss_{cycle} indirectly encourages structure preservation by enforcing translation maps to be one-to-one, but it does not guarantee structure preservation as is seen in Fig. 10. Incorporating Loss_{grad} and Loss_{air} suppress the type of large deformation in translation.

We combine these terms by taking the weighted sum with respect to the hyper-parameters λ :

$$\text{Loss}_G = \lambda_{cycle} \text{Loss}_{cycle} + \lambda_{adv} \text{Loss}_{adv} + \lambda_{grad} \text{Loss}_{grad} + \lambda_{idem} \text{Loss}_{idem} + \lambda_{air} \text{Loss}_{air} + \lambda_{tv} \text{Loss}_{tv}$$

and use stochastic gradient descent to find a (local) minimizer of the combined loss function.

Technical details

For efficiency, the intensity of CT images was clipped to $[-500, 200]$ HU, and scaled to $[-1, 1]$. That is, the pixels with an HU of less than -500 were all mapped to -1, and those with an HU of higher than 200 were all mapped to 1. When fed into the network, the images were cropped randomly around the center to a size of 480×384 pixels. This size was selected such that the body was always contained well inside the edges in order to avoid the boundary effects of convolutional neural networks in general.

For the generators G_* , we used an encoder–decoder network consisting of (i) One convolution layer with a 7×7 kernel with stride 1, (ii) followed by three down convolution layers with a 3×3 kernel with stride 2 and channels 32, 64 and 128, (iii) followed by 9 residual blocks with a 3×3 kernel with stride 1, (iv) followed by three up-sampling layers each consisting of an unpooling with stride 2 followed by a residual block with a 3×3 kernel with stride 1, (v) followed by a convolution layer with a 7×7 kernel with stride 1. Except for the last layer, we used the rectified linear unit for activation, and instance normalization³⁰ for normalization. The last layer was equipped with

the hyperbolic tangent as activation and without normalization. Layers (i),(ii) and (iv),(v) have skip connections³¹ to transfer the structure of the input image directly. To increase the stability, we added Gaussian noise of $\sigma = 0.05$ to the latent variable, which is just after the 4th residual block.

For the discriminators D_* , we used a typical down convolution network consisting of (i) A convolution layer with a 4×4 kernel with stride 1 and channels 32, (ii) followed by three down convolution layers with a 4×4 kernel with stride 2 and channels 64, 128 and 256, (iii) followed by a convolution layer with a 4×4 kernel with stride 1 and channels 256, (iv) followed by a convolution layer with a 4×4 kernel with stride 1 and channels 1. We used a leaky rectified linear unit with slope 0.2 for activation, and instance normalization for normalization in all but the last layer. We did not apply any normalization to the last layer. The receptive field of the network was 73×73 and each pixel in the output revealed the evaluation for the patch of this size in the input image. We also experimented with different network configurations by modifying the kernel size of each layer and the total number of layers, and thus with different receptive field sizes, and observed that the above configuration performs well.

In both the generators and the discriminators, it is important to use instance normalization without an affine transform; with an affine transform, we observed that the output images tended to have low voxel values in certain regions. The padding value for the first layer was selected to match the intensity of the air (-1 , in our case).

We chose the hyper-parameters empirically as follows:

$$\lambda_{cycle} = 10.0, \lambda_{adv} = 1.0, \lambda_{grad} = 0.1, \lambda_{tv} = 0.01, \lambda_{air} = 1.0, \lambda_{idem} = 1.0, \lambda_D = 1.0.$$

All networks were trained from scratch at a learning rate of 10^{-4} , with the Adam optimizer with a batch size of 1. We kept the same learning rate for the first 25 epochs, and linearly decayed the rate to zero over the next 25 epochs.

Note that for generators, minimizing Loss_{adv} means maximizing Loss_D , and for discriminators, minimizing Loss_D means maximizing Loss_{adv} . Generators and discriminators are adversarial, trying to beat each other. If the competition is nearly even, they both improve in a steady manner. Therefore, when training GANs, their strength must be balanced. There are several ways to help to maintain this balance: (i) tuning the weightings λ_{adv} and λ_D , (ii) using different loss functions (e.g., Wasserstein GAN with a gradient penalty³²), (iii) scheduling updates for the generator and discriminator (e.g., updating the generator only once for every five updates of the discriminator), (iv) tuning the degrees of freedom of the networks for the generators and discriminators, and (v) defining good stopping criteria. Although it was unfeasible to try all the possibilities, we

observed that the last one had the largest effect. We thus adjusted the number of channels in each network. Although Wasserstein GANs are believed to be very helpful, in our experiments we could not find a good configuration for our particular problem. Therefore, we decided to stick to the current loss function. Similarly, it was appropriate to set $\lambda_{adv} = \lambda_D$ and to update the generators and discriminators in equal frequency. The point at which learning stopped was also important. We noticed that if we trained too many epochs, the preservation of anatomical structures began to deteriorate. We watched the learning progress by visually inspecting the output, and decided to train 50 epochs for this study. However, this number should be dependent on the dataset. Establishing judicious stopping criteria remains for future research.

We conducted experiments with a personal computer equipped with a single GPU (Nvidia 1080Ti) and a CPU (Intel Core i7-6950X) with 132 GB memory, running Ubuntu 18.04.1 LTS. We implemented our algorithm with Python 3.6.6 and Chainer 5.0.0³³. Our codes are available on Github² The training required approximately 20 minutes per epoch (2795 iterations), and 13 hours for 50 epochs. The conversion required about 6 seconds for one volume of data (32 slices per second).

II.C. Evaluation method

The CBCT and PlanCT image pairs from 4 prostate cancer patients (v)–(viii) were used for the quantitative evaluation. Each PlanCT image was acquired just after each corresponding CBCT image was acquired, and the PlanCT images were aligned to the CBCT images by DIR (see §II.A.). The resulting SynPlanCT images were compared to the original CBCT and DefPlanCT images using the HU for statistic and visual inspections of the regions of interest (ROIs) from four different types of tissues (viz., prostate, bladder, muscle, and fat). For a quantitative evaluation of the muscle and fat regions, four slices were selected, one slice from each of the four patients. Four square ROIs with 10×10 pixels were positioned in the regions of the same soft tissue area (fat or muscle) in distant locations on a selected slice (Figure 1). Four slices at 3 mm intervals per patient were selected for the prostate region. Four slices at 6 mm intervals per patient were selected for the bladder region. One square ROI with 10×10 pixels was positioned in the regions of the same soft tissue area (prostate or bladder) on a selected slice. These ROIs were positioned on the corresponding slices and locations of the CBCT, SynPlanCT and DefPlanCT images. That is, 16 ROIs were positioned for each soft tissue to evaluate the distribution of the HU of each ROI. All the ROIs were selected from the region where DIR worked relatively well.

To determine the robustness of our method, we used images from patients (i)–(iv). For each

²<https://github.com/shizuo-kaji/UnpairedImageTranslation>

evaluation slice, we produced five SynPlanCT images from five network models trained with the same structure and hyper-parameters.

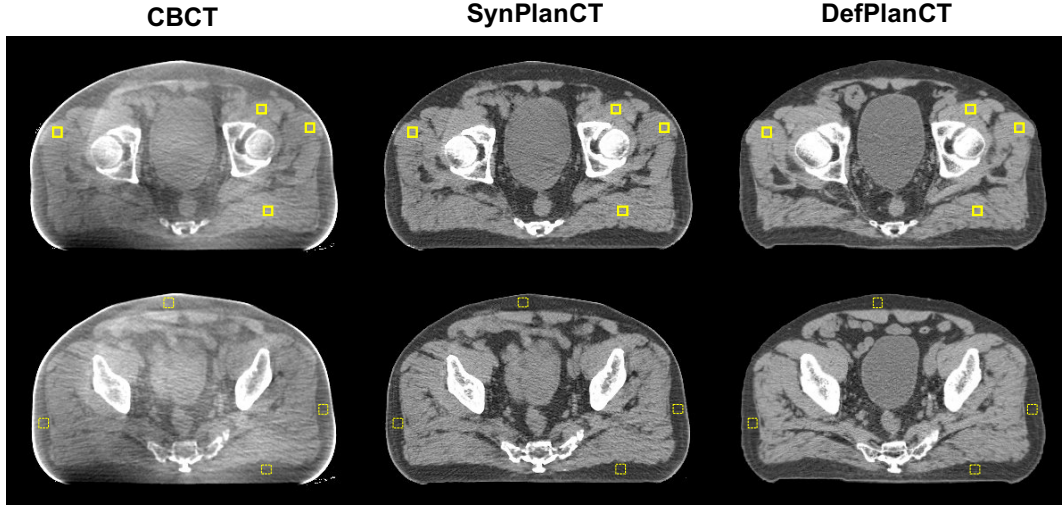


Figure 1: Example of evaluating the ROI distribution: (Upper left) Four muscle ROIs (solid square) placed on a selected slice of CBCT for test patient (viii), (Upper middle) corresponding ROIs placed on a corresponding slice of SynPlanCT, and (upper right) corresponding ROIs placed on a corresponding slice of DefPlanCT. (Lower left) Four fat ROIs (dotted square) placed on another slice of the CBCT, (lower middle) corresponding ROIs placed on a corresponding slice of the SynPlanCT, and (lower right) corresponding ROIs placed on a corresponding slice of the DefPlanCT; The display window range was set to $(-400, 0)$ HU for CBCT and $(-200, 200)$ HU for SynPlanCT and DefPlanCT.

III. Results

III.A. Comparison of Image qualities and Preservation of anatomical structures

The axial, sagittal, and coronal slices of CBCT, SynPlanCT, and PlanCT for two representative cases (test patients (i) and (ii)) are shown in Figure 2. The image quality of SynPlanCTs for all three planes show substantial improvement in terms of voxel values, spatial uniformity, artifact suppression, compared to those of the original CBCT.

As shown in Figure 3, the edge sharpness and structure were preserved in not only the large bulky tissues, such as the rectum and bladder, but also in small isolated structures, such as the small intestine and intestinal gas. High-frequency artifacts such as streaks and rings could not be completely removed, but they were considerably suppressed. In this study, despite learning with only axial slices, owing to computational limitations, there was no outstanding problem in the continuity of the structure and voxel values in the other two planes (coronal and sagittal), as

shown in Figure 2.

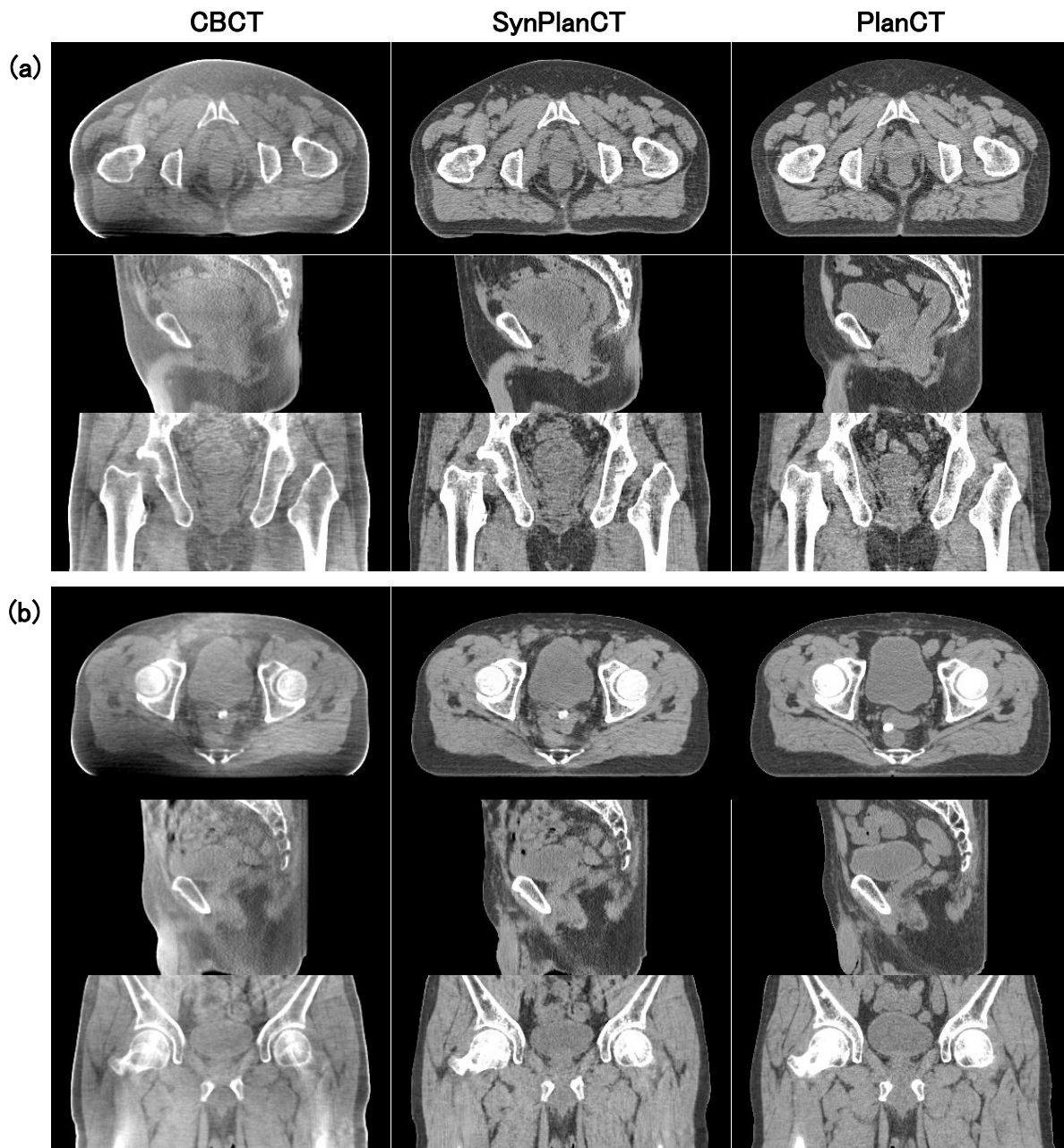


Figure 2: Comparison of the image quality among CBCT, SynPlanCT, and PlanCT: (a) test patient (i) and (b) test patient (ii). For each patient, the images in the top, middle, and bottom row are axial, coronal, and sagittal views, respectively. The images on the left, middle, and right are CBCT, SynPlanCT and PlanCT, respectively. The display window range was set to $(-400, 0)$ HU for CBCT and $(-200, 200)$ HU for SynPlanCT and PlanCT.

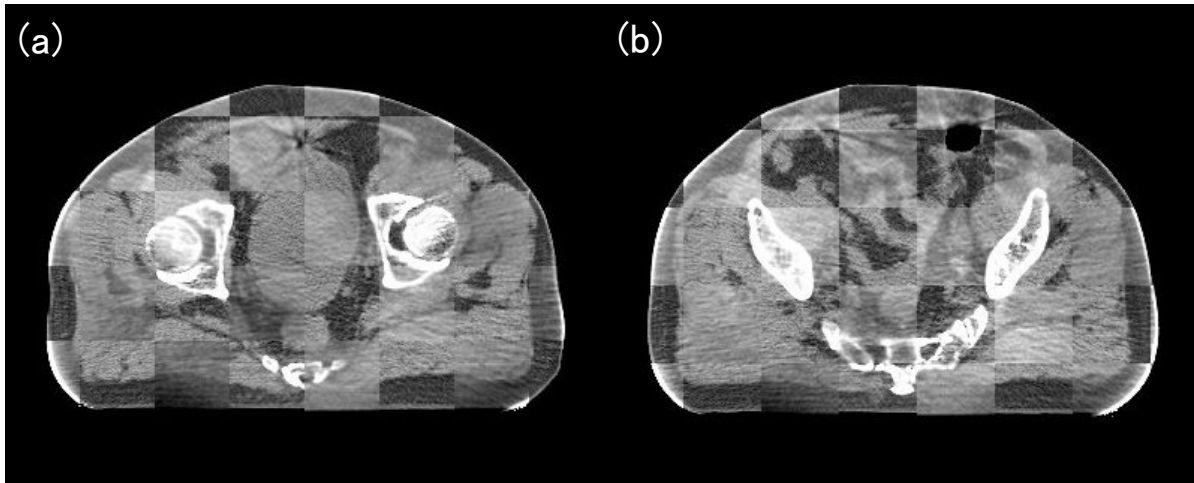


Figure 3: Checkerboard images of a CBCT image and SynPlanCT image: (a) bladder and rectum slice, and (b) small intestine slice. The display window range was set to $(-400, 0)$ HU for CBCT and $(-200, 200)$ HU for SynPlanCT.

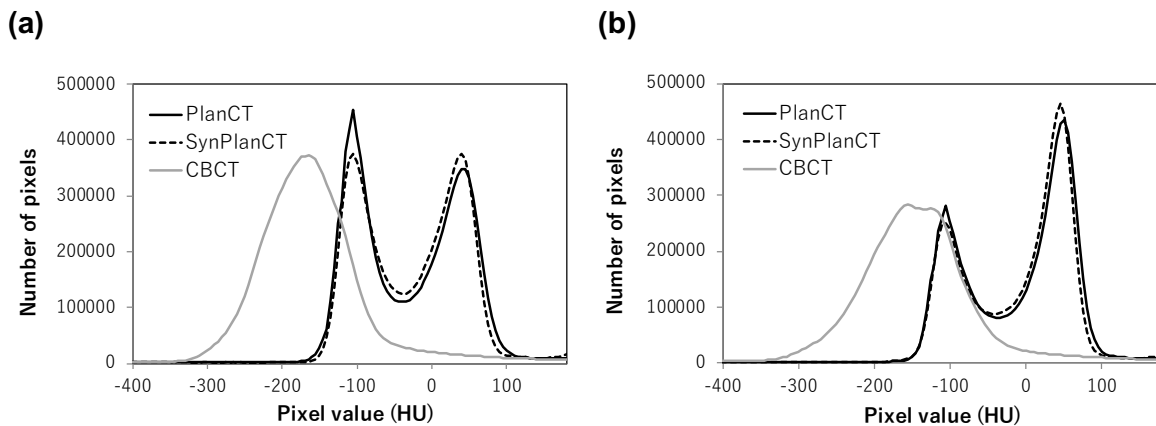


Figure 4: Image histograms for the 3D volume of CBCT (grey line), corresponding volume of SynPlanCT (dotted black line) and corresponding volume of PlanCT (solid black line) for representative two patients. (a) patient (vi) and (b) patient (vii).

III.B. Quantitative evaluation

The histograms of the 3D volume of CBCT, SynPlanCT, and PlanCT images for two representative cases (test patients (vi) and (vii)) are shown in Figure 4. The histograms of SynPlanCT images are much closer to those of the PlanCT images, with better differentiation between the fat and muscle, compared to those of the CBCT images. The mean and standard deviation of the HU of the 16 ROIs positioned in the four evaluation tissues in DefPlanCT, SynPlanCT, and CBCT are summarized in Table 1. For each tissue type, 16 ROIs were selected from four patients. The difference in the average HU for the four evaluation tissues between SynPlanCT and DefPlanCT (muscle: 7HU, fat: 2HU, prostate: 14HU, bladder: 4HU) were substantially suppressed compared to those between the

original CBCT and DefPlanCT (muscle: 190HU, fat: 110HU, prostate: 194HU, bladder: 166HU). Figure 5 shows comparisons among CBCT, SynPlanCT, and DefPlanCT in the distribution of the HU of each ROI positioned in the four evaluation tissues. The width indicates the ratio of the pixels with a specific HU. We observe that the HU distributions of SynPlanCT are much closer to those of DefPlanCT than those of CBCT for all the ROIs positioned in the four evaluation tissues.

		DefPlanCT (HU)	SynPlanCT (HU)	CBCT (HU)
Muscle	mean	52	45	-138
	sd	14	17	23
Fat	mean	-104	-106	-214
	sd	13	16	43
Prostate	mean	33	19	-161
	sd	23	22	19
Bladder	mean	8	4	-158
	sd	18	18	17

Table 1: Mean and standard deviations of the HU values of the ROIs in the four evaluation tissues in DefPlanCT, SynPlanCT, and CBCT.

Assessment of the quality of an image in the absence of a reference image is called as non-reference image quality assessment (NR IQA)³⁴. The NR IQA metrics are defined for natural images but not for medical purposes. In fact, we tried some metrics including Natural Image Quality Evaluator (NIQE) and Blind/Referenceless Image Spatial Quality Evaluator (BRISQUE) only to find that they were highly dependent on the ROIs and were thus not robust. Instead, we propose a simple metric to assess the resolution and contrast of the images, which we found to be very stable:

$$\text{SelfSSIM}(img) = \text{SSIM}(img, blur),$$

where SSIM is the Structural Similarity³⁵ and *blur* is the Gaussian blur of *img* with $\sigma = 3$. If an image *img* has good spatial resolution and contrast, it should have a large difference if blurred. Therefore, the lower the SelfSSIM(*img*) is, the more the quality of *img* is. Table 2 shows the mean and standard deviation of SelfSSIM for 30 ROIs from each of CBCT, DefPlanCT, and SynPlanCT of size 120×120 located at the center. The HU values are scaled to [0,255] and we used an implementation of SSIM in OpenCV 4.1.0³⁶.

There was an ROI with specifically low HU in the prostate for the SynPlanCT images, as shown in the ROI 13 of Figure 5(c). Figure 6 compares the CBCT and SynPlanCT images synthesized by applying a network model (m1) to test patient (viii). We found that the voxel values of the region indicated by the arrow on the SynPlanCT images were lower than the surrounding prostate region

	DefPlanCT (HU)	SynPlanCT (HU)	CBCT (HU)
mean	0.575	0.688	0.799
sd	0.0080	0.0095	0.0159

Table 2: Mean and standard deviation of SelfSSIM of the ROIs in the four evaluation tissues in DefPlanCT, SynPlanCT, and CBCT.

(Figure 6(b)), and the region was included in ROI 13 partially. Low signal artifact was observed originally in the prostate region of the CBCT image, as indicated by the arrow in Figure 6(a), and it seemed that the low signal artifact was emphasized with a higher contrast on SynPlanCT (Figure 6(b)). However, it is difficult to determine whether this low signal is an artifact or a tissue feature. It may be important in terms of structural preservation to preserve subtle contrasts, when it is difficult to demarcate artifacts from tissues.

Figure 7 compares the image quality of the artifact region between CBCT and SynPlanCT and the distributions of the HU of the selected evaluation ROIs for the representative two slices. Evaluation ROI (20×50 pixels) was placed on the fat region of the selected slice of CBCT for test patient (vi) and the corresponding ROI was placed on the corresponding slice of SynPlanCT of the same patient (Figure 7(upper row)). Another evaluation ROI (20×15 pixels) was placed on the muscle region of the selected slice of CBCT for test patient (viii) and the corresponding ROI was placed on the corresponding slice of SynPlanCT of the same patient (Figure 7(lower row)). The streak and ring artifacts were substantially suppressed visually for both the cases. For the distributions of HU, large differences of HU between the tissues and artifacts were observed as different peaks for CBCT; however, such differences of HU were hardly observed for SynPlanCT and DefPlanCT in both the cases.

Figure 8 compares the distributions of the HU of one ROI positioned in each of the four evaluation tissues of each of the five SynPlanCT images, synthesized using the five network models trained with the same structure and hyper-parameters (m1–m5) and those of PlanCT. Note that the SynPlanCT images used in Figure 2–5 and Table 1 were synthesized by applying the network model (m1). The average HU differed by 10 HU or less for all of the four evaluation tissues in the five SynPlanCT images.

IV. Discussion

We developed a CycleGAN-based method to synthesize PlanCT-like images from the CBCT images. In contrast to the previous work using PlanCT on the same patient as prior information,

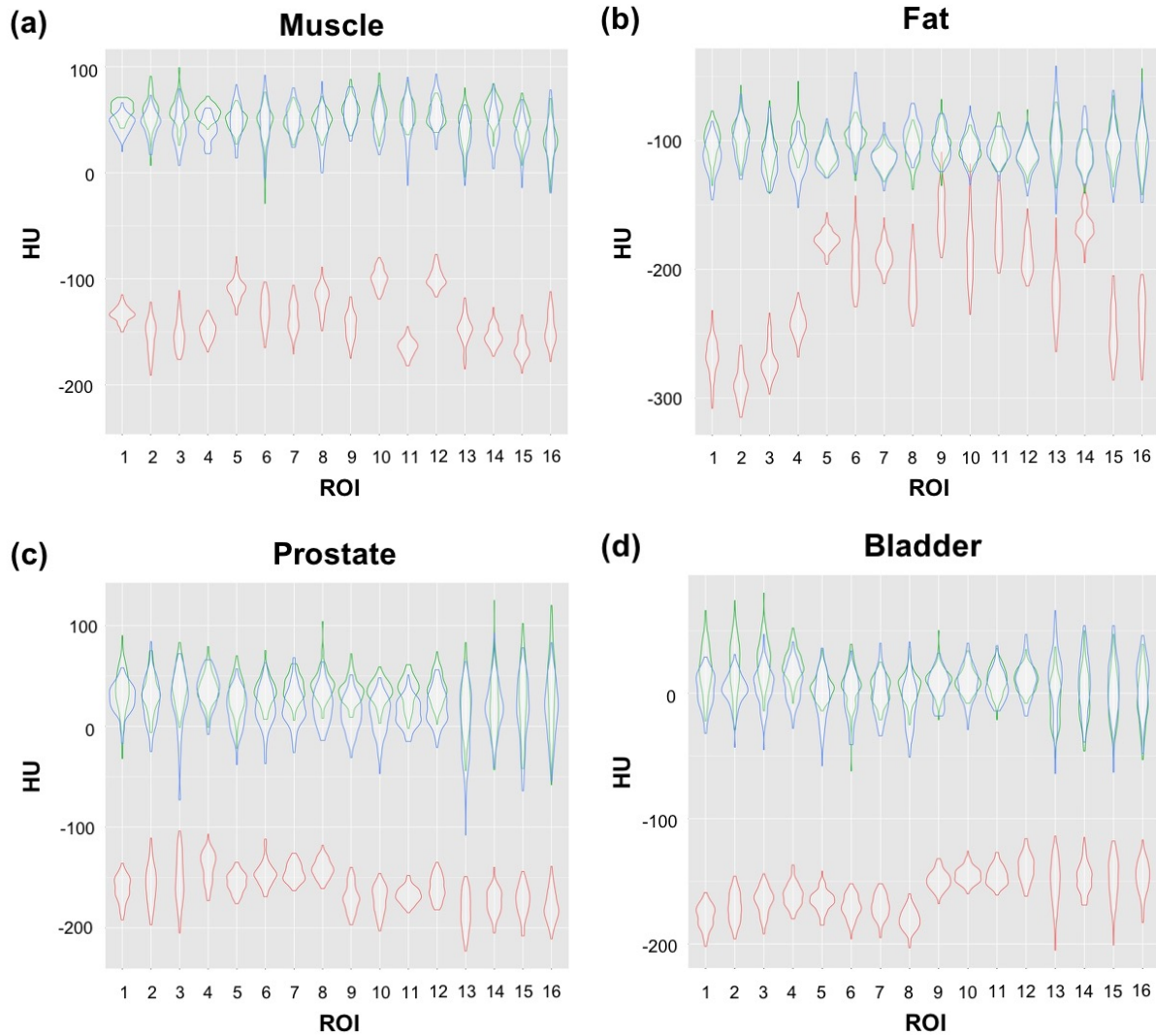


Figure 5: Comparison of the distribution of the HU values in (a) muscle, (b) fat, (c) prostate, and (d) bladder ROIs among CBCT (red), SynPlanCT (blue), and DefPlanCT (green). ROI(1-4), ROI(5-8), ROI(9-12), and ROI(13-16) are selected for test patients (v), (vi), (vii), and (viii), respectively. The width indicates the ratio of the pixels with a specific HU.

the proposed method does not, in principle, require accurate spatially aligned CBCT and PlanCT volume pairs from the same patients. In this study, models were trained with CBCT and PlanCT images of the same patients, and these images were rigidly registered to include bodies of all patients in a cropped calculation area around the center, in the size of 480×384 pixels for efficient calculation. During the training process of CycleGAN, the discriminators were provided randomly selected unpaired and unaligned images, rather than aligned paired images. Therefore, registration between CBCT and PlanCT should not affect the image quality of synthesized PlanCT. The

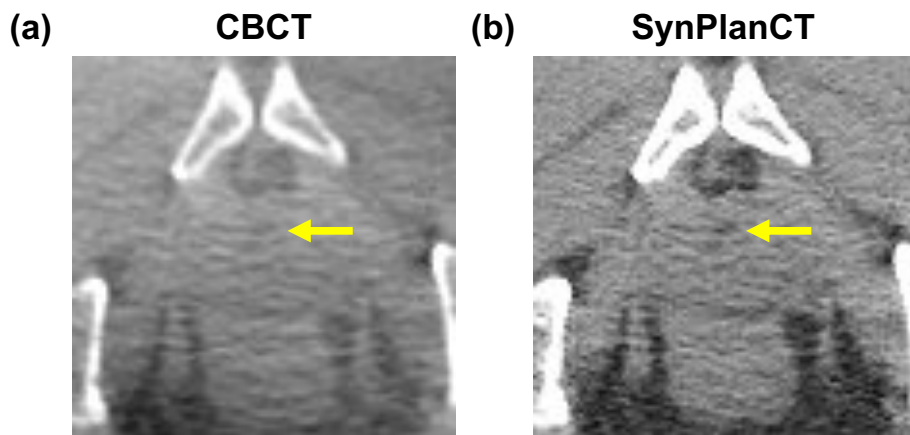


Figure 6: Example of regions with particularly low HU in a prostate: (a) Region with lower HU than the surrounding prostate region is indicated by the arrow on the selected slice of CBCT for test patient (viii). (b) Region with lower HU than the surrounding prostate region is indicated by the arrow on the corresponding slice of SynPlanCT of the same patient. The indicated regions were partially included in ROI 13 of Figure 5(c).

amount of training data does affect the quality of synthesized PlanCT. To see this, the 16 patients for training were divided into two groups. Then, the network model was trained with the CBCT images of eight patients and the PlanCT images of the other eight patients. This model showed similar improvement in the voxel values, spatial uniformity, and artifact suppression on the SynPlanCT images, but the structures were incorrectly synthesized in some slices. The failure to preserve the structures may be caused by over-learning due to the reduction by half of the learning data.

In evaluating a medical application for a DNN, the following three points of view are important. (i) Accuracy: the output of the method is close to the ground truth, which is often clinically unavailable. (ii) Precision: the method is robust and produces stable outputs. In general, DNN-based methods inevitably involve randomness when initializing the weights of the networks and during the learning process. Hence, even with the same parameters and the same dataset, their outcome can never be the same. (iii) Generalization: the method works with different datasets acquired in different ways. To evaluate the accuracy of our method ideally, we compare the SynPlanCT images with the PlanCT images acquired simultaneously with the CBCT images, although these pairs are obviously unavailable. Hence, in this study, we assessed the accuracy of the output SynPlanCT by visually inspecting The preservation of the anatomical structures compared with CBCT, and the image quality compared with PlanCT.

Preserving anatomical structures is crucial for image-improvement methods using unpaired and unaligned CBCT and PlanCT datasets. In a previous work using PlanCT as prior information,

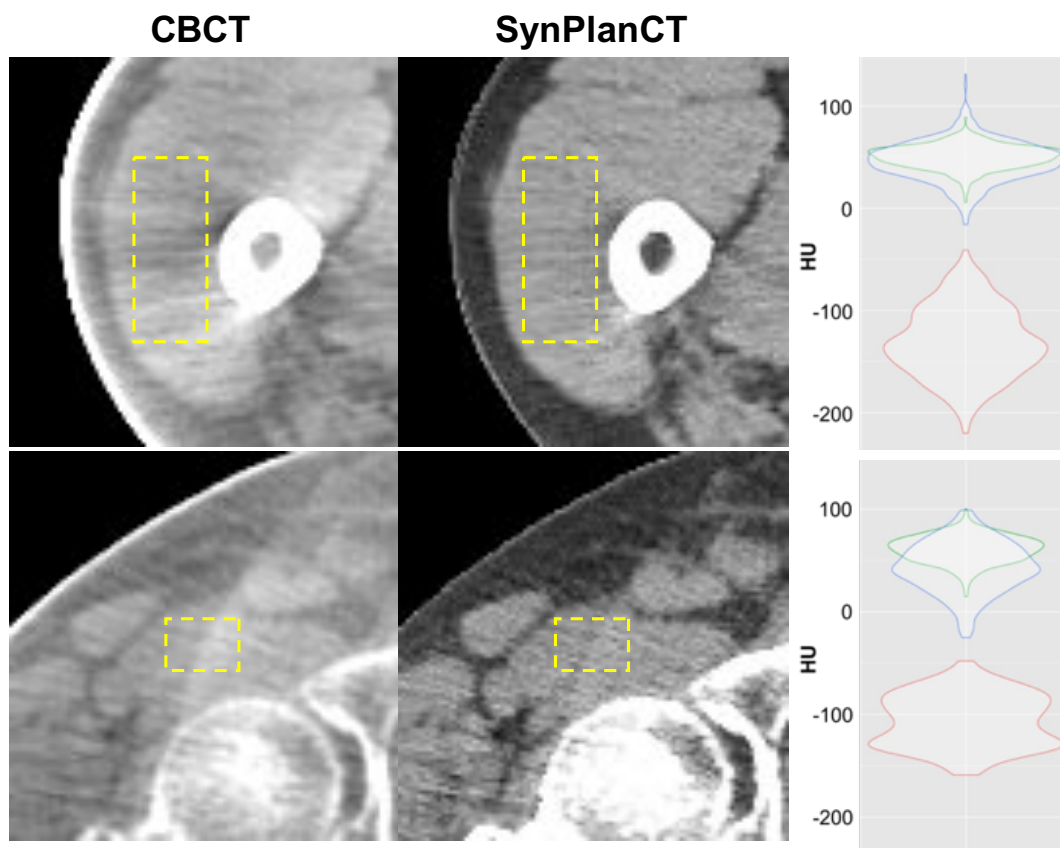


Figure 7: Comparison of the image quality of the artifact region for CBCT and SynPlanCT. (Upper-left) Evaluation ROI (20×50 pixels) was placed on the fat region of a selected slice of CBCT for test patient (vi), (upper-middle) corresponding ROI placed on a corresponding slice of SynPlanCT of the same patient, and (Upper-right) the distributions of the HU of the selected evaluation ROIs for CBCT (red), SynPlanCT (blue), and DefPlanCT (green). (Lower-left) Evaluation ROI (20×15 pixels) was placed on the muscle region of the selected slice of CBCT for test patient (viii), (lower-middle) corresponding ROI placed on the corresponding slice of SynPlanCT of the same patient and (lower-right) the distributions of the HU of the selected evaluation ROIs for CBCT (red), SynPlanCT (blue), and DefPlanCT (green). The width indicates the ratio of the pixels with a specific HU.

high-frequency artifacts such as streaks, blurred edges, deformations, and missing anatomical structures were left as problems to be solved^{15,16,17,18}. In this study, the image quality of CBCT improved while suppressing high-frequency artifacts and preserving the anatomical structures of CBCT. Designing the size of the receptive field of the discriminator is important for preserving the structure and concurrently converting the voxel values. When the receptive field is set too large, learning with a DNN is influenced by the structure and placement of the organs of individual patients. That is, it requires overlearning. On the other hand, when the receptive field is too small, the local structural pattern cannot be detected, and only the voxel values are converted, ignoring the structure. The 73×73 receptive fields of the discriminator used in this study can detect

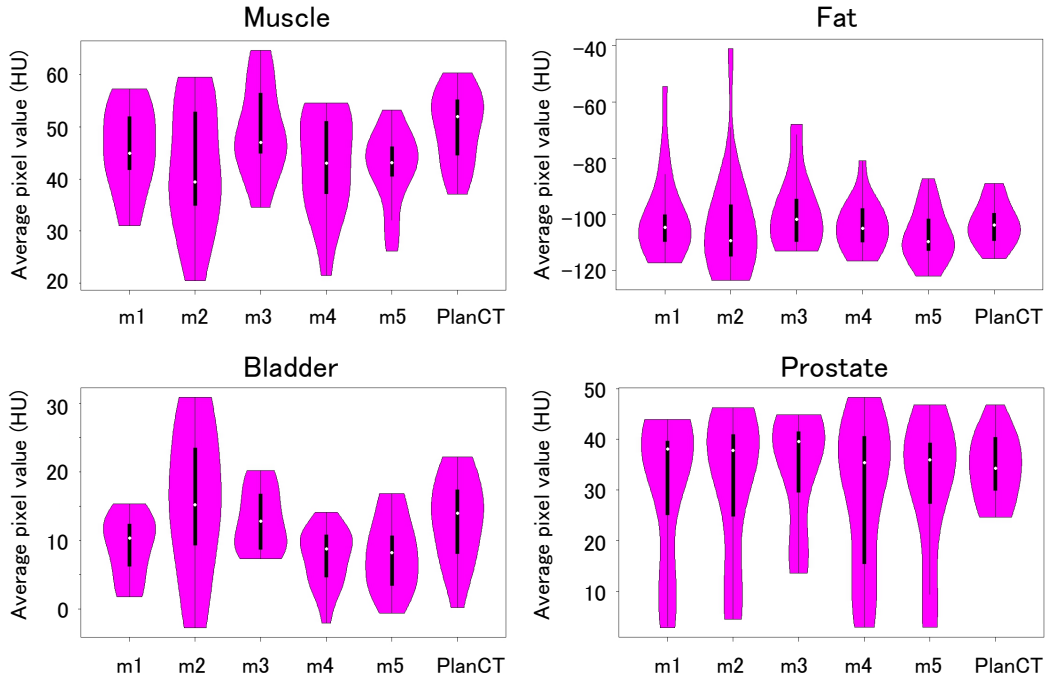


Figure 8: Comparison of the distribution of the HU of one ROI positioned in each of the four evaluation tissues for each of the five SynPlanCT images from five network models trained with the same structure and hyper-parameters (m1–m5) and those of PlanCT for comparison. The width indicates the ratio of the pixels with a specific HU.

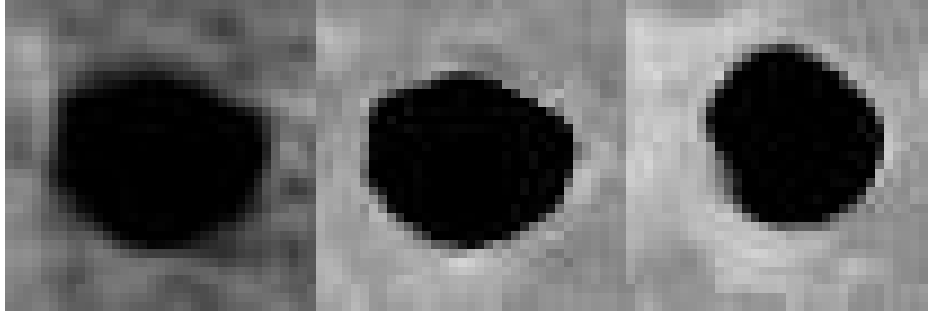


Figure 9: Comparison of a ROI containing air (left) Original CBCT (middle) SynPlanCT with $\lambda_{adv} = 1.0$, $\lambda_{grad} = 0.1$ (right) SynPlanCT with $\lambda_{adv} = 0$, $\lambda_{grad} = 0$. The shape of the air region is altered in the right image.

typical local structural patterns commonly found in all patients, enabling the conversion of voxel values while preserving the structure (Figure 3). Another important factor which contributes to the preservation the anatomical structures is our design of the loss functions for the neural networks (see §II.B.). In particular, if we set $\lambda_{air} = 0$ and $\lambda_{grad} = 0$, some anatomical structures of CBCT were altered in SynPlanCT. Figure 9 shows an example of a ROI from CBCT and SynPlanCT produced by a mode trained with $\lambda_{adv} = 1.0$, $\lambda_{grad} = 0.1$ and one with $\lambda_{adv} = 0$, $\lambda_{grad} = 0$. They show exactly the same coordinates but the shape of the air region was altered in SynPlanCT with

$$\lambda_{adv} = 0, \lambda_{grad} = 0 .$$

Moreover, despite learning with only axial slices, due to computational limitations, there was no outstanding problem in the continuity of the structure and voxel values in the coronal and the sagittal planes (Figure 2). Such continuity along the other two planes is evidence that the anatomical structure was correctly preserved within the axial images. In future work, we will investigate how learning directly with volume data can affect the continuity of voxel values and the preservation of anatomical structures.

The image quality of SynPlanCT showed substantial improvement in terms of voxel values, spatial uniformity, and artifact suppression compared to those of the original CBCT. The variation of distributions of HU among fat ROIs was larger than that of other tissues (muscle, prostate, bladder) as shown in Table 1 and Figure 5. This result means that various artifacts, such as rings streaks, and shading have a stronger effect on fat, spreading closer to body surface, than in the muscle, prostate, and bladder, located relatively near the center of the body, and indeed the artifacts were effectively suppressed by the proposed method. In this study, voxel values of CBCT and PlanCT images were clipped to $[-500, 200]$ for efficient calculation. Thus, the voxel values of bone, which are more than 200 HU, were not evaluated quantitatively. In future work, we will expand the range of voxel values used for learning and quantitatively evaluate the improvement in voxel values of bone.

In order to assess the precision of our method, we compared five models trained with the same structure and hyper-parameters, but trained with different random initial weights and stochastic gradient descent. We observed acceptable fluctuation of less than 10 HU (Figure 8). Note that we did observe on one occasion that models trained with the same hyper-parameters produced totally different images. Although it is customary in medical applications of DNNs to present results from only the best models, we here provide an extreme example in which the generators (trained with $\lambda_{grad} = 0$ and $\lambda_{air} = 0$) completely failed to learn a meaningful mapping and produced totally distorted images (see Figure 10). In our method, this type of failure was mitigated by introducing additional loss terms λ_{grad} , λ_{tv} , and λ_{air} as discussed in §II.B., which helped to increase the overall robustness. Even after proper training, it is impossible to ensure that the DNN will always produce feasible outputs. Thus, it is more important to detect and alert the user when a failure may have occurred. We can use the cycle consistency Loss_{cycleA} (see §II.B.) as a measure of the soundness of our networks' output. Such failures in training (e.g., see Figure 10) can be detected as a high value of Loss_{cycleA} , namely, when this is more than three times that when training was successful. Recall that Loss_{cycleA} is a summary of the difference in the voxel values of the CBCT image x and the cyclically translated image $G_{P \rightarrow C}(G_{C \rightarrow P}(x))$. We can look directly at a so-called difference image



Figure 10: Example of a failed SynPlanCT image from some network model: (left) original CBCT image, and (right) failed SynPlanCT image.

$G_{P \rightarrow C}(G_{C \rightarrow P}(x)) - x$ to locate where the violation of cycle consistency occurred. To visualize the violation, it is more suitable to look at the difference in the gradient rather than in the voxel values. As such, we define the *cycle difference image* as

$$\|(\partial_1(G_{P \rightarrow C}(G_{C \rightarrow P}(x))), \partial_2(G_{P \rightarrow C}(G_{C \rightarrow P}(x))))\|_2 - \|(\partial_1(x), \partial_2(x))\|_2,$$

where ∂_1, ∂_2 are Sobel's gradient operators²⁹. If both generators $G_{C \rightarrow P}$ and $G_{P \rightarrow C}$ work perfectly, the cycle difference image should constantly be zero. Thus, we can use this cycle difference image to check how and where the generators may have failed. To demonstrate this, we selected a pair of successfully learned models $G_{C \rightarrow P}$ and $G_{P \rightarrow C}$ and an input image x containing metal seeds and a couch, which were not seen in the training data. The cycle difference image clearly indicates anomalous objects that were not learned during training (Figure 11). This result shows that we can use the cycle difference as a simple safeguard against failures both in training and inference.



Figure 11: Example of cycle difference: (left) original CBCT image containing metal seeds, (middle) cyclically translated image, and (right) their difference in the gradient.

There are two possible directions in which our method can be generalized. We believe that

the proposed method works properly with CBCT and PlanCT image datasets acquired in other institutions. In addition, the proposed method should improve the image quality of organs other than the pelvis. These two directions will be pursued in future research.

V. Conclusion

We developed a synthetic approach based on CycleGAN to produce SynPlanCT images from CBCT images. The proposed approach relies only on unpaired and unaligned CBCT and PlanCT images for training. The image quality of the synthesized PlanCT images substantially improved compared to those of the original CBCT. The anatomical structures of the original CBCT were well preserved in SynPlanCT. In order to demonstrate the robustness of our method, we compared five models trained with the same structure and hyper-parameters, and observed an acceptable fluctuation of less than 10 HU. The proposed method may be applied directly to 3D CBCT images reconstructed from a commercial CBCT scanner with a high computational efficiency. The proposed method may enable soft tissue details to be more easily visualized.

Acknowledgments

Kaji was partially supported by JST PRESTO, Grant Number JPMJPR16E3 Japan. Nawa was partially supported by a JSPS Grant-in-Aid for Young Scientists (B), 17K15799. Imae was partially supported by a JSPS Grant-in-Aid for Scientific Research (C), 18K07667. Nakamoto was partially supported by a JSPS Grant-in-Aid for JSPS Fellows, 18J00599, and a Grant-in-Aid for Early-Career Scientists, 18K15625. Ohta was partially supported by a JSPS Grant-in-Aid for Early-Career Scientists, 18K15583.

We would like to thank Editage (www.editage.jp) for English language editing.

Conflict of Interest Statement

This study was partially funded by Canon Medical Systems Corporation.

References

- [1] D. Letourneau, A. A. Martinez, D. Lockman, D. Yan, C. Vargas, G. Ivaldi, and J. Wong, Assessment of residual error for online cone-beam CT-guided treatment of prostate cancer patients, *Int. J. Radiat. Oncol. Biol. Phys.* **62**, 1239–46 (2005).

- [2] M. Gukenberger, J. Meyer, D. Vordermark, K. Baier, J. Wilbert, and M. Flentje, Magnitude and clinical relevance of translational and rotational patient setup errors: a cone-beam CT study, *Int. J. Radiat. Oncol. Biol. Phys.* **65**, 934–942 (2006).
- [3] D. A. Jaffray, J. H. Siewerdsen, J. W. Wong, and A. A. Martinez, Flat-panel cone-beam computed-tomography for image-guided radiation therapy, *Int. J. Radiat. Oncol. Biol. Phys.* **53**, 1337–1349 (2002).
- [4] X. Wang, J. Li, P. Wang, K. Yuan, G. Yin, and B. Wan, Image guided radiation therapy boost in combination with high-dose-rate intracavitary brachytherapy for the treatment of cervical cancer, *Brachytherapy* **8**, 122–127 (2016).
- [5] X. Fave, D. Mackin, J. Yang, J. Zhang, D. Fried, P. Balter, D. Followill, D. Gomez, A. K. Jones, F. Stingo, J. Fontenot, and L. Court, Can radiomics features be reproducibly measured from CBCT images for patients with non-small cell lung cancer?, *Med. Phys.* **42**, 6784–6797 (2015).
- [6] J. E. van Timmeren, R. T. H. Leijenaar, W. van Elmpt, B. Reymen, and P. Lambin, Feature selection methodology for longitudinal cone-beam CT radiomics, *Acta. Oncol.* **56**, 1537–1543 (2017).
- [7] S. Kim, S. Yoo, F. F. Yin, E. Samei, and T. Yoshizumi, Kilovoltage cone-beam CT: comparative dose and image quality evaluation in partial and full-angle scan protocols, *Med. Phys.* **37**, 3648–3659 (2010).
- [8] M. Stock, M. Pasler, W. Birkfellner, P. Homolka, R. Poetter, and D. Georg, Image quality and stability of image-guided radiotherapy (IGRT) devices: a comparative study, *Radiother. Oncol.* **93**, 1–7 (2009).
- [9] C. Kurz, F. Kamp, Y. Park, C. Zollner, S. Rit, D. Hansen, M. Podesta, G. C. Sharp, M. Li, M. Reiner, J. Hofmaier, S. Nepl, C. Thieke, R. Nijhuis, U. Ganswindt, C. Belka, B. A. Winey, K. Parodi, and G. Landry, Investigating deformable image registration and scatter correction for CBCT-based dose calculation in adaptive IMPT, *Med. Phys.* **43**, 5635–5646 (2016).
- [10] D. Paquin, D. Levy, and L. Xing, Multiscale registration of planning CT and daily cone beam CT images for adaptive radiation therapy, *Med. Phys.* **36**, 4–11 (2009).
- [11] S. B. Park, F. C. Rhee, J. I. Monroe, and J. W. Sohn, Spatially weighted mutual information image registration for image guided radiation therapy, *Med. Phys.* **37**, 4590–4601 (2010).

- [12] U. Stankovic, L. S. Ploeger, M. van Herk, and J. J. Sonke, Optimal combination of anti-scatter grids and software correction for CBCT imaging, *Med. Phys.* **44**, 4437–4451 (2017).
- [13] A. Sisniega, W. Zbijewski, A. Badal, I. S. Kyprianou, J. W. Stayman, J. J. Vaquero, and J. H. Siewerdsen, Monte carlo study of the effects of system geometry and antiscatter grids on cone-beam CT scatter distribution, *Med. Phys.* **40**, 051915 (2013).
- [14] M. Sun and J. M. Star-Lack, Improved scatter correction using adaptive scatter kernel superposition, *Phys. Med. Biol.* **55**, 6695–6720 (2010).
- [15] L. Shi, T. Tsui, J. Wei, and L. Zhu, Fast shading correction for cone beam CT in radiation therapy via sparse sampling on planning CT, *Med. Phys.* **44**, 1796–1808 (2017).
- [16] H. S. Kidar and H. Azizi, Assessing the impact of choosing different deformable registration algorithms on cone-beam CT enhancement by histogram matching, *Radiat. Oncol.* **13**, 217 (2018).
- [17] A. Oyama, S. Kumagai, N. Arai, T. Takata, Y. Saikawa, K. Shiraishi, T. Kobayashi, and J. Kotoku, Image quality improvement in cone-beam CT using the super-resolution technique, *J. Radiat. Res.* **59**, 501–510 (2018).
- [18] S. Kida, T. Nakamoto, M. Nakano, K. Nawa, A. Haga, J. Kotoku, H. Yamashita, and K. Nakagawa, Cone beam computed tomography image improvement using a deep convolutional neural network, *Cureus* **10** (2018).
- [19] M. Mazurowski, M. Buda, A. Saha, and M. Bashir, Deep learning in radiology: an overview of the concepts and a survey of the state of the art, in *arXiv:1802.08717*, 2018.
- [20] T. Higaki, Y. Nakamura, F. Tatsugami, T. Nakaura, and K. Awai, Improvement of image quality at CT and MRI using deep learning, *Jpn. J. Radiol.* **29**, 1–8 (2018).
- [21] P. Isola, J. Zhu, T. Zhou, and A. A. Efros, Image-to-image translation with conditional adversarial networks, in *2017 IEEE Conference on Computer Vision and Pattern Recognition, CVPR 2017, Honolulu, HI, USA, July 21-26, 2017*, pages 5967–5976, 2017.
- [22] D. Nie, R. Trullo, J. Lian, C. Petitjean, S. Ruan, Q. Wang, and D. Shen, Medical image Synthesis with context-aware generative adversarial networks, in *Medical Image Computing and Computer Assisted Intervention (MICCAI)*, volume 10435, pages 417–25, 2017.

- [23] J. Zhu, T. Park, P. Isola, and A. A. Efros, Unpaired Image-to-Image Translation Using Cycle-Consistent Adversarial Networks, in *IEEE International Conference on Computer Vision, ICCV 2017, Venice, Italy, October 22-29, 2017*, pages 2242–2251, 2017.
- [24] J. M. Wolterink, A. M. Dinkla, M. H. F. Savenije, P. R. Seevinck, C. A. T. van den Berg, and I. Išgum, Deep MR to CT Synthesis Using Unpaired Data, in *Simulation and Synthesis in Medical Imaging*, edited by S. A. Tsafaris, A. Gooya, A. F. Frangi, and J. L. Prince, pages 14–23, Cham, 2017, Springer International Publishing.
- [25] X. Liang, L. Chen, D. Nguyen, Z. Zhou, X. Gu, M. Yang, J. Wang, and S. Jiang, Generating synthesized computed tomography (CT) from cone-beam computed tomography (CBCT) using CycleGAN for adaptive radiation therapy, *Physics in Medicine & Biology* **64**, 125002 (2019).
- [26] N. Otsu, A Threshold Selection Method from Gray-Level Histograms, *IEEE Transactions on Systems, Man and Cybernetics* **9**, 62–66 (1979).
- [27] S. Klein, M. Staring, K. Murphy, M. A. Viergever, and J. P. W. Pluim, Elastix: a toolbox for intensity-based medical image registration, *IEEE. Trans. Med. Imaging.* **29**, 196–205 (2010).
- [28] X. Mao, Q. Li, H. Xie, R. Y. K. Lau, Z. Wang, and S. P. Smolley, On the Effectiveness of Least Squares Generative Adversarial Networks, in *arXiv:1712.06391*, 2018.
- [29] I. Sobel and G. Feldman, An isotropic 3x3 image gradient operator, in *Stanford Artificial Intelligence Project (SAIL)*, 1968.
- [30] D. Ulyanov, A. Vedaldi, and V. S. Lempitsky, Improved Texture Networks: Maximizing Quality and Diversity in Feed-Forward Stylization and Texture Synthesis, in *2017 IEEE Conference on Computer Vision and Pattern Recognition, CVPR 2017, Honolulu, HI, USA, July 21-26, 2017*, pages 4105–4113, 2017.
- [31] O. Ronneberger, P. Fischer, and T. Brox, U-Net: Convolutional Networks for Biomedical Image Segmentation, in *Medical Image Computing and Computer-Assisted Intervention - MICCAI 2015 - 18th International Conference Munich, Germany, October 5 - 9, 2015, Proceedings, Part III*, pages 234–241, 2015.
- [32] I. Gulrajani, F. Ahmed, M. Arjovsky, V. Dumoulin, and A. C. Courville, Improved Training of Wasserstein GANs, in *Advances in Neural Information Processing Systems 30*, edited by

- I. Guyon, U. V. Luxburg, S. Bengio, H. Wallach, R. Fergus, S. Vishwanathan, and R. Garnett, pages 5767–5777, Curran Associates, Inc., 2017.
- [33] S. Tokui, K. Oono, S. Hido, and J. Clayton, Chainer: a Next-Generation Open Source Framework for Deep Learning, in *Proceedings of Workshop on Machine Learning Systems (LearningSys) in The Twenty-ninth Annual Conference on Neural Information Processing Systems (NIPS)*, 2015.
- [34] S. Xu, S. Jiang, and W. Min, No-reference/Blind Image Quality Assessment: A Survey, *IETE Technical Review* **34**, 223–245 (2017).
- [35] Z. Wang, A. C. Bovik, H. R. Sheikh, and E. P. Simoncelli, Image Quality Assessment: From Error Visibility to Structural Similarity, *IEEE TRANSACTIONS ON IMAGE PROCESSING* **13**, 600–612 (2004).
- [36] Itseez, Open Source Computer Vision Library, <https://github.com/itseez/opencv>, 2015.